Direct visualization of colloid transport across a natural heterogeneous fractured rock surface

Oshri Borgman[1,2], Avraham Be'er[1], Noam Weisbrod[1]

[1]Zuckerberg Institute for Water Research, Jacob Blaustein Institutes for Desert Research, Ben-Gurion University of the Negev, Midreshet Ben-Gurion 8499000, Israel
[2]Univ Rennes, CNRS, Géosciences Rennes, UMR 6118, 35000, Rennes, France

Key Points:

- Colloid transport experiments were performed with a chemically and physically heterogeneous natural fracture surface
- We compared direct fluorescence visualization of colloid transport with their breakthrough curves
- Varying surface topography leads to preferential flow and early colloid breakthrough

Corresponding author: Oshri Borgman, oshri.borgman@univ-rennes1.fr

Abstract

Colloid transport in fractured rock formations is an important process impacting the fate of pollutants in the subsurface. Despite intensive and outstanding research on their transport phenomena, the impact of small-scale surface heterogeneity on colloid behavior at the fracture scale remains difficult to assess. In particular, there is relatively little direct experimental evidence on the impact of natural fracture surface heterogeneity on colloid transport. To investigate this, we developed an experimental setup allowing the direct visualization of fluorescent colloid transport, in a flow cell containing a chalk rock sample. We used samples containing both a natural fracture surface and an artificially made smooth surface from the same chalk core. We characterized the roughness and chemical composition of both surface types. From the experiments, we obtained direct images of colloid transport over the surfaces, the colloid breakthrough curves at the outlet of the flow cell, and the residual deposition of colloids on the rock surface. The natural fracture surface exhibited larger physical and chemical heterogeneity than the smooth surface. The aperture variability across the natural fracture surface led to preferential flow and colloid transport, as well as their earlier breakthrough from the flow cell, compared to the artificially made surface. Our experimental setup can be used to further investigate the link between surface heterogeneity, both chemical and physical, on colloid transport and deposition in natural rock fractures.

1 Introduction

The fate of solutes and pollutants in the environment is highly dependent on their ability to migrate from their source point to other locations, where they might have undesirable effects. Fractured rock formations are ubiquitous in the subsurface and may potentially function as favorable conduits for solutes and pollutants, due to the formation of highly permeable and extensive fracture networks (Sahimi, 2011). The importance of flow and transport in fracture networks is even greater in rock formations with low matrix permeability, such as the chalk formation found in southern Israel's Negev Desert (Weisbrod et al., 1999). In such conditions, fractures are effectively the only conduits for water and solutes within the rock formation (Nativ et al., 1999; Tran et al., 2020).

Colloid and colloid-facilitated contaminant transport, in fractured rock, is highly relevant to environmental transport processes. During colloid-facilitated transport, soluble pollutants are attached to (or form) colloids, which in turn, can migrate great distances over short time periods. This phenomenon has long been identified as a mechanism for enhanced pollutant transport in the environment (McCarthy & Zachara, 1989). Colloid-facilitated transport is also specifically linked to the enhanced migration of radionuclides from nuclear test sites (Kersting et al., 1999; Zavarin et al., 2013), constituting a major concern for the environmental safety of subsurface nuclear waste repositories (Missana et al., 2008; Albarran et al., 2013). The transport phenomena of the colloids themselves are also important on their own, for example, in the transport of bacteria and viruses to the groundwater (Weisbrod et al., 2013) or the migration of the now ubiquitous microplastics (Horton & Dixon, 2018; Brewer et al., 2021).

The surface of rock fractures is characterized by irregular roughness at the microscale, i.e., the length scale between several micrometers and one millimeter. This roughness impacts the aperture and permeability at the single fracture scale and may also affect the flow characteristics in fracture networks (Méheust & Schmittbuhl, 2001; Berkowitz, 2002; Bodin et al., 2003). One result of this surface heterogeneity is flow channeling, so that the solution flows mostly through the more permeable regions of the fracture aperture, thereby significantly enhancing solute transport in fractured media (Tsang & Neretnieks, 1998; Brown et al., 1998). Experiments and models of solute transport in granite fractures have directly shown the importance of characterizing fracture surface roughness for solute transport modeling. A simplified model, which did not consider the surface

roughness, did not describe well the experimentally obtained solute breakthrough curves (Stoll et al., 2019). In the context of colloid transport, the anisotropic distribution of fracture apertures in the mean flow direction (i.e., longer correlation length of apertures in the general flow direction) has been shown to increase the dispersion of low-density particles (Chrysikopoulos & James, 2003; Boutt et al., 2006). Although nanoscale roughness can also impact colloid retention on surfaces (Rasmuson et al., 2017), it was not measured here, and thus, it will not be considered in the following.

Fracture surfaces also exhibit chemical heterogeneity due to their diverse mineral composition. Typically, they are partially coated by deposited material, resulting from long-term flow and transport processes along the surfaces (Thoma et al., 1992; Weisbrod et al., 2000). These deposits may include metal oxides, precipitated salts, and clay minerals, and thus, they may alter the characteristics of the fracture surface with relation to the bulk rock matrix (Weisbrod et al., 1999). Nevertheless, the effects of the surface chemical or mineralogical composition on colloid retention remain unclear. It was found that colloid retention and deposition on fracture surfaces can occur even under electrostatically repulsive conditions (Alonso et al., 2009; Albarran et al., 2013), and in some cases, it was impossible to establish a correlation between the presence of specific minerals on the surface and colloid deposition (Chinju et al., 2001; Albarran et al., 2013).

Several studies have used artificially cut, and sometimes polished, fracture surfaces in colloid transport experiments (Chinju et al., 2001; Zavarin et al., 2013; Albarran et al., 2013). As shown by Stoll et al. (2016), in colloid transport experiments in a flow cell with two surface types (a natural rock sample and an acrylic surface), the surface roughness plays an important role in colloid retention. In addition, the qualitative and quantitative analyses of colloid transport behavior were mostly based on breakthrough curve measurements and analyses, and the colloid retention and deposition patterns were based on post-experimental analyses of the rock surface. Rodrigues and Dickson (2015) presented a hybrid approach, using natural fractured rock samples and their transparent acrylic replicas to study bacterial transport. Their comparison of the breakthrough curves of the natural and the transparent synthetic fractures demonstrated the impact of fracture surface material on bacterial retention, with the transparent fractures demonstrating preferential bacterial transport. The coupling of both the transport dynamics and the overall transport behavior for natural fracture samples, therefore, remains a challenge.

In most previous works, crystalline rocks were used as the fractured media, due to their relevance to specific countries and locations (Albarran et al., 2013; Stoll et al., 2016). However, carbonate rocks are also important media for contaminant transport in many cases (Froidevaux et al., 2010; Mondal & Sleep, 2012; Medici et al., 2019). For example, in southern Israel's Negev Desert, sedimentary rock and, specifically, chalk are common in subsurface formations. It was shown that fractures play a major role in these formations and facilitate contaminant and colloid transport (Zvikelsky & Weisbrod, 2006; Kurtzman et al., 2007; Tang & Weisbrod, 2010; Cohen & Weisbrod, 2018; Tran et al., 2020). Therefore, it is of great interest to use this type of rock in colloid and contaminant transport studies, to better understand and predict the behavior at the regional scale.

Here, we simultaneously study colloid transport and deposition, by direct visualization, and the overall transport behavior shown by their breakthrough curves, in the same experimental flow cell. The goal is to study the impact of chemical and physical fracture surface heterogeneity on colloid transport, breakthrough, and deposition, in an experimental setup that includes a naturally fractured rock sample. Our results show the direct link between fracture surface topography, flow channeling, and preferential colloid transport, and their breakthrough behavior.

2 Methods

2.1 Experimental setup

We used a unique experimental system comprising a natural chalk sample encased in a flow cell, with a transparent glass top cover. We mounted the flow cell on the stage of an AXIO Zoom.V16 fluorescence microscope (Carl Zeiss Microscopy, Jena, Germany), equipped with a PlanNeoFluar Z objective, an HXP 120 V light source, and an Axiocam 506 monochrome camera (Fig. 1). The flow cell's inlet was connected to the colloid suspension vial and to another bottle containing the background solution. A stopcock was used to switch between the colloid suspension and the background solution. The flow cell's outlet was connected to a peristaltic pump (Gilson Minipuls 3, Middleton, WI, USA), which drew liquid at a constant flow rate. The peristaltic pump was connected to a fraction collector (Spectra/Chrom CF-1, Houston, TX, USA), which collected eluent samples at constant time intervals.

The body of our custom-designed flow cell was 3D-printed in Polyamide 12 nylon (Shapeways NL, Eindhoven, The Netherlands), and contained a rectangular cavity to hold the rock sample. The flow cell cover plate was made of glass. Two holes were drilled into the glass to insert inlet and outlet tubes for colloid suspension and wash (background) solution. The full cavity dimensions were 66, 36, and 20 mm in length, width, and depth, respectively. The actual rock sample size was then slightly reduced to fit the cavity. Polydimethylsiloxane (PDMS, Polymer-G, Gvulot, Israel) was used to fill the small gap between the rock sample and the flow cell cavity, and to hold the sample in place.

2.2 Natural rock samples

We used rock samples taken from coreholes drilled into the Avdat Group chalk formation in Israel's central Negev Desert (Nativ et al., 1999). Some cores were recovered as intact cylinders, while others were naturally fractured. From the naturally fractured core samples, we separated the two parts of the fractured core and kept one of them, to be used as a fracture surface for transport experiments. We used non-fractured cores to artificially prepare rock surfaces that were not physically or chemically altered by mechanical processes or groundwater flow. The surfaces of the naturally fractured rock samples were characterized by large variation in surface topography and mineral deposition, which we described as having high heterogeneity (HH). The artificially created rock surface was characterized by low heterogeneity (LH), both physically and chemically.

All rock samples were cut to fit the cavity 3-D printed flow cell, so that the rock surface was exposed, and a half-fracture was formed between the rock surface and the cell's glass cover. We note that in this manner, we were unable to reproduce the complete structure of a natural fracture, with its two opposing rough walls. More specifically, in our system, we did not create zero-aperture points in which the rock surface meets the cover glass plate. However, our setup still enabled us to represent the natural fracture roughness in a transparent flow cell, which allowed direct fluorescence imaging. Also, we expect that these zero-aperture points would have more strongly increased the impact of the rough surfaces' physical heterogeneity compared to that of the smooth surfaces.

We measured the surface topography of the rock samples using an Olympus LEXT OLS5000 3D scanning laser microscope (Olympus, Japan). We obtained spatial resolutions of 10, 10, and 0.1 μm in the x, y, and z coordinates, respectively. We transformed the measured elevation levels of the rock surface to the apertures of the experimental fracture cell—the vertical distances between the rock surface and the glass cover. We achieved this by measuring the distance between the bottom of the glass cover and the rock surface at a specific location. We then used this point as a reference and transformed the elevation field to a map of fracture apertures. The calculated fracture apertures over the

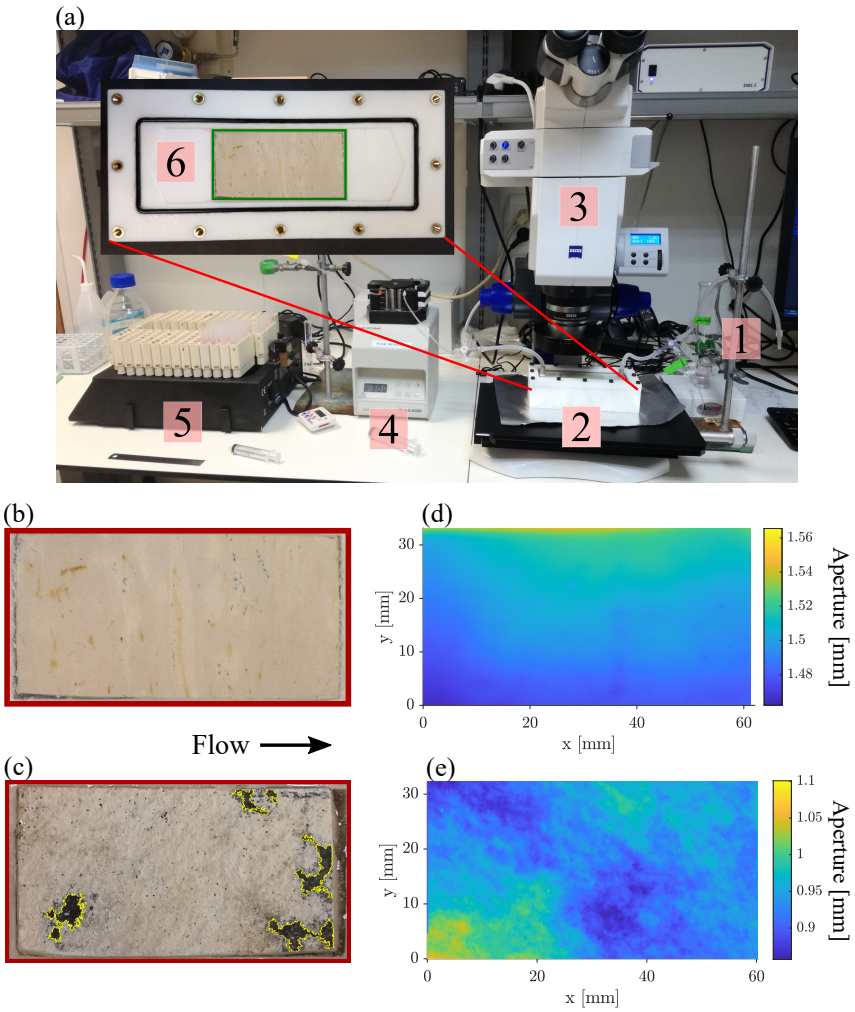

Figure 1. (a) The experimental setup included: (1) a pulse suspension and wash solution; (2) a flow cell; (3) a fluorescence microscope; (4) a peristaltic pump; and (5) a fraction collector. A top-view close-up of the flow cell, showing the chalk sample in the green frame (a6). The samples used were: (b) an artificially created rock surface from a non-fractured rock core; and (c) a natural fracture surface characterized by higher roughness and large dark-colored patches, which we attribute to deposited minerals on the surface (see the regions outlined in yellow). The arrow indicates the flow direction. Calculated fracture apertures—the vertical distances between the rock and the glass cover—are shown for an artificially created rock surface (d) and a natural fracture surface (e).

rock surfaces are presented in Fig. 1(d)–(e). The minimum and maximum apertures were 1.46 and 1.57 mm for the LH sample, and 0.86 and 1.10 mm for the HH sample, respectively.

To quantify the surface topography of the rock surface, we used standard measures of surface roughness. The arithmetic mean roughness was calculated as (Kurra et al., 2015)

$$\mathrm{Ra} = \frac{1}{n_\mathrm{p}} \sum_{i=1}^{n_\mathrm{p}} |z(i) - \overline{z}| \,, \tag{1}$$

where n_p is the number of pixels in the image of the surface, and $z(i)$ and $\overline{z}$ are the elevation of a single pixel and the mean elevation, respectively. The root mean squared roughness was calculated as (Stoll et al., 2016)

$$\mathrm{Rq} = \sqrt{\frac{1}{n_\mathrm{p}} \sum_{i=1}^{n_p} (z(i) - \overline{z})^2}. \tag{2}$$

Higher Ra values indicate a higher average difference between the surface height values and their mean, while higher Rq values indicate a wider distribution.

To characterize the mineralogical composition of the rock surface, an EDS elemental analysis of small samples from both rock surfaces was performed using a Quanta 200 scanning electron microscope (SEM; FEI, USA). The EDS analysis was performed in areas that seemed to be of interest from visual inspection of the surfaces—for example, the black-colored regions outlined in yellow in Fig. 1(c). Analyses were also performed for samples from artificially-created surfaces, to study the composition of the bulk rock.

2.3 Colloid transport experiments

2.3.1 Background solution and colloid suspension

We used a background solution of 10 mM NaCl throughout the experiments. We prepared colloid suspensions with 10 mg/L of orange fluorescent F-8820 FluoSpheres® carboxylate modified latex microspheres, with a 1-μm nominal bead diameter (Molecular Probes, USA). Fresh suspensions were made for each experiment from a 1-g/L stock and transferred to a 20-ml vial, which was placed on a magnetic stirrer 30 min prior to the injection into the flow cell.

2.3.2 Experimental protocol

Before the experiments, the rock samples were saturated and equilibrated with the background solution (see Section 2.3.1) overnight. In addition, we passed several fracture aperture volumes of the background solution through the flow cell before the beginning of the experiment, to equilibrate the surface with the solution, at a flow rate of 0.1 ± 0.01 cm^3/min. This flow rate was maintained throughout the experiment, and the resulting mean flow velocities varied from 0.150–0.293 cm/min (see Table 1 for details).

A typical transport experiment included two stages: (1) a colloid suspension pulse of between 4.5 and 5.2 fracture aperture volumes at a constant concentration was injected into the flow cell; and (2) the flow cell was washed with the background solution, until the surface fluorescence did not change, indicating that deposited colloids could not be removed under the prevalent flow conditions.

During each experiment, we collected fluorescence images using the AXIO Zoom microscope. To obtain a complete image of the rock surface, we collected a panorama composed of 15 tiles (5×3, length×width). The size of each tile was 15.31×13.88 mm^2 or 2360×2140 pixels (length × width), with a pixel size of 6.486×6.486 μm^2. Since

Table 1. Characteristics of the flow cells and the experimental conditions.

Experiment name[a]	Typical fracture aperture b [cm]	Fracture aperture volume V_f [cm^3]	Flow rate Q [cm^3/min]	Mean flow velocity $\overline{u}$ [cm/min]	Re[b]	Pe[c]
LH	0.15	3.78	0.1	0.167	0.0434	9.27×10^4
LH-b	0.15	3.78	0.09	0.150	0.0390	8.33×10^4
HH	0.094	2.36	0.1	0.267	0.0435	9.39×10^4
HH-b	0.094	2.36	0.11	0.293	0.0477	10.20×10^4

[a] – LH, LH-b: low heterogeneity rock surface; HH, HH-b: high heterogeneity rock surface. See Section 2.3.2 for details.
[b] – Reynolds number.
[c] – Péclet number.

the microscope was equipped with a manually driven stage, such acquisition typically took ∼5 min to complete. The main acquisition parameters of the optical system were excitation filter wavelengths of 540-552 nm, emission filter wavelengths of 575-640 nm, a beam splitter wavelength of 560 nm, and an exposure time of 500 milliseconds.

We performed two experiments with low heterogeneity samples (experiments LH and LH-b) where we used, for each experiment, a newly prepared artificially created rock surface. For the high heterogeneity experiments (experiments HH and HH-b), we used the same rock sample and reversed the flow direction between experiments. For the latter case, we thoroughly washed the flow cell after the first experiment, to remove residual fluorescence from deposited colloids.

2.3.3 Flow and transport characteristics

To characterize the flow, we calculated the Péclet and Reynolds numbers, defined as

$$\mathrm{Pe} = \frac{\overline{u}b}{D}, \tag{3}$$

and

$$\mathrm{Re} = \frac{\rho\overline{u}b}{\eta}, \tag{4}$$

respectively. Here $\overline{u}$ [LT^{-1}] is the mean flow velocity in the fracture, b [L] is the typical fracture aperture, ρ [ML^{-3}] is the water density, η [ML^{-1}T^{-1}] is their dynamic viscosity, and D [L^{2}T^{-1}] is the colloid diffusion coefficient, which we estimated using the Stokes-Einstein equation

$$D = \frac{k_\mathrm{B}T}{6\pi\eta d_\mathrm{p}}, \tag{5}$$

where k_B [L^{2}MT^{-2}K^{-1}] is the Boltzmann constant, T [K] is the temperature, and d_p [L] is the colloid diameter.

2.4 Data analysis

2.4.1 Colloid transport over the rock surface

To qualitatively show the colloid transport over the rock surface, we used the fluorescence images, captured at various times, and applied the following procedure. First, we converted the color images exported by the microscope's software to grayscale images. We then subtracted the background (time zero) image from the other images. Next,

we used a global threshold to binarize the images and obtained a mask of the regions covered by the fluorescent colloids. Finally, we combined the binarized images taken at different times, to show the evolution of fluorescence in the flow cell with time.

2.4.2 Colloid breakthrough curves

We quantified the fluorescence emission intensity of eluent samples collected during the experiments using an Infinite 200 plate reader (Tecan, Männedorf, Switzerland), using excitation and emission wavelengths of 500 and 560 nm, respectively. The fluorescence intensities of the eluent samples were compared to the intensity of the pulse suspension, to obtain the relative concentration C/C_0, where C and C_0 are the specific sample and pulse concentrations, respectively.

We estimated the colloid mass recovery from the breakthrough curves by directly calculating the ratio between the total pulse fluorescence and the total eluted fluorescence. The total fluorescence of the pulse was calculated as

$$\Phi_{\text{pulse}} = \phi_{\text{pulse}} V_{\text{pulse}}, \tag{6}$$

where ϕ_{pulse} (arbitrary units) is the fluorescence measured in the pulse suspension, and V_{pulse} [L^3] is the total volume of the pulse. The recovered fluorescence was calculated as

$$\Phi_{\text{rec}} = \sum \phi_i V_i, \tag{7}$$

where ϕ_i is the fluorescence measured in each eluted sample i, and V_i [L^3] is the sample volume. The mass recovery was then calculated as $\Phi_{\text{rec}}/\Phi_{\text{pulse}}$.

2.4.3 Residual colloid surface concentration

To quantify the residual colloid concentration on the rock surface, we took fluorescence images of the surface at the end of the experiment (after the wash stage, Section 2.3.2). To reduce the noise in the calculation, we averaged the fluorescence intensity in windows of 10 × 10 pixels. Next, we used a calibration curve (see below) to transform the intensity values to surface colloid concentrations (colloid mass per rock surface area). Finally, we calculated the longitudinal concentration profiles, by averaging along transects perpendicular to the flow direction,

$$\overline{C_{\text{s}}}(x) = \frac{1}{w} \int C_{\text{s}}(x, y) dy, \tag{8}$$

where C_{s} [ML^{-2}] is the surface concentration, w is the rock sample width [L], and x and y are the coordinates parallel and perpendicular to the flow direction, respectively.

To obtain the surface concentration calibration curve, we first placed a colloid suspension drop with a known concentration on the rock surface, under the fluorescence microscope, and measured the area of the fluorescent mark created on the surface. Using the known volume and concentration in the drop, we could determine the overall mass of colloids on the surface. We then calculated the colloids' overall surface mass concentration (in dimensions of [ML^{-2}]). Next, we obtained a representative value of the fluorescence intensity per unit of rock surface area by averaging the intensity in 10 equally sized sub-regions of each mark. The calibration curve was then linearly fitted to the plot of surface concentrations and fluorescence intensity values.

3 Results and discussion

3.1 Direct visualization of fluorescent colloid transport

We observed a strong impact of the fracture surface topography on the advancing colloid front, for different surface heterogeneities under the same flow rate. With the nat-

ural fracture rock surface (experiment HH; Table 1), a preferential colloid transport path was created along the rock surface, due to the variation in the fracture topography. On the other hand, with the artificially created rock surface (experiment LH; Table 1), the colloid front was relatively smooth. In Fig. 2(a)–(b), we show the dynamics of colloid transport over the surface during the first part of the experiment, until shortly after their breakthrough at the outlet.

In some regions, we did not observe a significant fluorescent cover over the surface, at the time of breakthrough or immediately after it. In these regions, fluorescence was apparent only in a few interspersed pixels, and thus, it was not observed in the full image. These regions appear in black in Fig. 2(a)–(b), and they are most apparent for the high heterogeneity surface (Fig. 2(b)). We mostly attribute this behavior to the heterogeneous velocity field that delayed the arrival of colloids to regions where the fracture aperture was narrower and velocity was expected to decrease (Brown et al., 1998; Stoll et al., 2019). At later times, not shown in Fig. 2(a)–(b), the fluorescence over most of the rock surface increased, indicating that colloids eventually covered the entire surface. However, the reduced fluorescence is also attributed, in part, to the dark coating on some parts of the natural fracture rock surface (see the yellow-outlined regions in Fig. 1c). While we could not verify this, the surface's dark color appeared to reduce the fluorescence intensity of colloids flowing over (or deposited on) it. Nevertheless, the coated areas accounted for only a part of the regions where fluorescence was low or late-arriving; therefore, we maintain that preferential flow still significantly contributed to the earlier breakthrough of colloids in the natural fracture surface experiments.

3.2 Colloid breakthrough curves and mass recovery

We observed earlier breakthrough of colloids with the natural fracture rock surfaces (experiments HH and HH-b; Table 1) than with the artificially created surfaces (experiments LH and LH-b; Table 1), as we show in Fig. 2(c). We attribute this behavior to the varied topography of the natural rock surfaces, which encouraged the emergence of preferential flow and colloid transport (see Fig. 2(b)).

To compare the breakthrough behavior between experiments, we compared the number of fracture aperture volumes needed to reach the normalized concentration of $C/C_0 = 0.5$. In our experiments, the colloid breakthrough curves reached $C/C_0 = 0.5$ after 1.34-1.51 fracture aperture volumes, for natural fracture rock surfaces (experiments HH and HH-b). We observed a higher retardation of colloids with the artificially created fracture surfaces (experiments LH and LH-b), where the number of fracture aperture volumes required to reach $C/C_0 = 0.5$ were 2.54 and 1.97 for experiments LH and LH-b, respectively. These values stand in contrast to some reported experiments of artificial colloid transport in fractured rock, where colloids traveled faster than the averaged water flow velocity, resulting in earlier breakthrough times compared with conservative solute tracers (Becker et al., 1999; Zvikelsky & Weisbrod, 2006; Albarran et al., 2013; Stoll et al., 2016).

These differences can be partly explained by the relatively large aperture in our experimental setup (∼1 mm), compared to the colloid diameter (1 μm). The main reasons for early colloid breakthrough in fractures are the limited diffusion of the colloids (within the suspension and into the solid matrix), their finite size (size exclusion), and their charge (Zvikelsky & Weisbrod, 2006). Together, these characteristics do not allow the colloids to flow across the entire (parabolic) velocity profile of the fracture, and specifically, they limit the colloids from accessing low-velocity flow trajectories near the fracture surface. Consequently, the effective colloid velocity is often higher than the average water velocity, by a factor that depends on the ratio between the colloid diameter

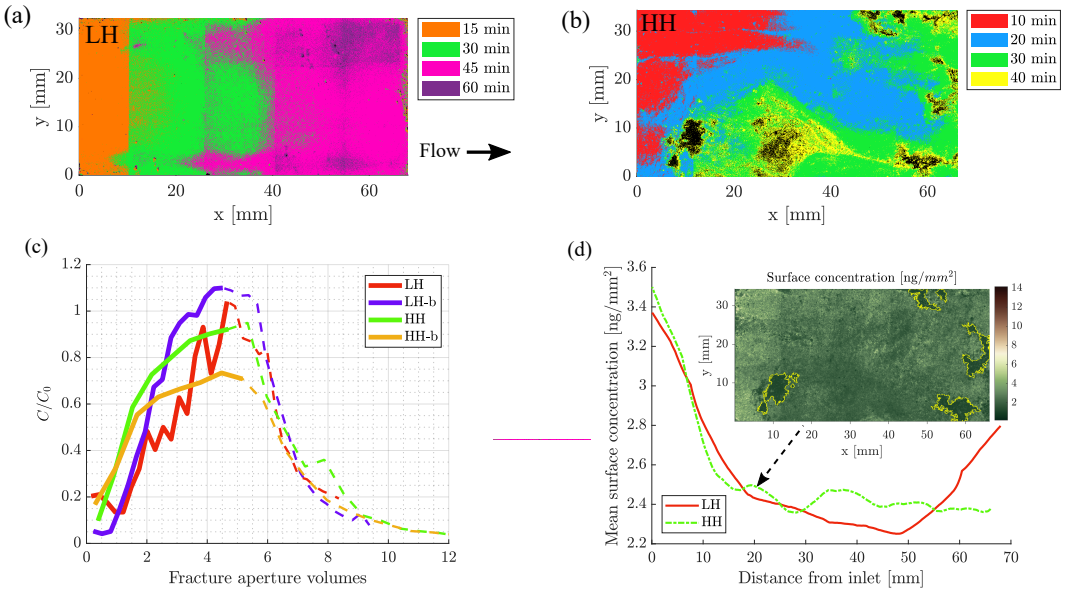

Figure 2. Higher fracture surface heterogeneity led to preferential colloid transport. We show the map of the fluorescent colloid cover over the rock surface at different times, for two experiments with varying degrees of surface heterogeneity: (a) an artificially created rock surface (LH) and (b) a natural fracture surface (HH). The colors represent the time at which colloids covered different parts of the surface. Black color indicates regions not covered by fluorescence. We used different time intervals for the two experiments due to the difference in flow velocities (see Table 1). The arrow indicates the flow direction. (c) The normalized colloid breakthrough curves (C/C_0 = outflow colloid concentration divided by the initial pulse concentration) from the flow cell, for experiments with an artificially created rock surface (LH) and a natural fracture surface (HH). The breakthrough curves are plotted against the number of fracture aperture volumes that passed through the cell. The solid part of the lines represents the pulse duration, and the dashed part represents the wash with background solution. (d) Surface concentration profiles of the colloids at the end of the experiments for artificially created (LH) and natural fracture (HH) surfaces. The inset shows an image of the natural fracture surface at the end of the experiment, highlighting regions of apparently very low colloid deposition in dark green, measured from the fluorescence intensity. The regions delimited by the yellow line correspond to the yellow-delimited regions in Fig. 1(c).

d_p [L] and the fracture aperture b [L], such that (James & Chrysikopoulos, 2003)

$$U_{\text{eff}} = \overline{U}\left[1 + \frac{d_p}{b} - \frac{1}{2}\left(\frac{d_p}{b}\right)^2\right], \tag{9}$$

where U_{eff} [LT^{-1}] and $\overline{U}$ [LT^{-1}] are the effective colloid velocity and the average water velocity, respectively. In our experimental setup, $d_p/b \sim 1.001$, so we expected negligible acceleration of colloids with respect to the average water velocity. In most other studies cited here, the fracture aperture was smaller than in our experimental setup, possibly increasing the colloids' effective velocity and driving their early breakthrough. We note that we assumed that the average solution velocity would be determined by the flow rate and cross-section aperture area, although we did not verify this with a conservative tracer.

We also note the relatively low maximum concentration in the breakthrough curve of experiment HH-b, and we cannot conclude what caused this behavior. However, we stress that the emphasis here is the difference in the colloid arrival time and its relation to the surface topography.

The recovery values $\Phi_{\text{rec}}/\Phi_{\text{pulse}}\times 100$ [%] we obtained were 89.2, 107.9, 87.3, and 82.7%, for experiments LH, LH-b, HH, and HH-b, respectively. Therefore, we could not find a trend in the relation between the mass recovery values and the sample type.

To determine the x-axis of Fig. 2(c), we multiplied time by the flow rate and divided by the total fracture aperture volume to obtain the number of fracture aperture volumes that passed through the flow cell.

3.3 Surface heterogeneity and colloid deposition

The longitudinal profiles of residual colloid concentrations on the rock surface at the end of the experiment exhibited higher concentrations close to the inlet, which decreased along the flow direction (Fig. 2(d)). In addition, we did not observe a notable difference in the residual colloid deposition between the two surface types, although the natural fracture surface (HH) was characterized by a slightly higher roughness than the artificially created fracture surface (LH). We calculated Ra = 11.5 and 26.3 μm, and Rq = 14.0 and 33.5 μm, for the LH and HH surfaces, respectively. In the LH experiment, we also observed an increase in concentration near the outlet. This may have been an artifact related to hydrodynamic edge effects, in which the flow profile changed due to the transition from the rock surface to the enclosing flow cell structure, and the thin layer of PDMS used to seal the rock sample in place (see Section 2.1).

While the long-range topographical variation between our samples is visually apparent, it is not clear whether the differences in the roughness parameters, Ra and Rq, would have caused the differences in colloid retardation and deposition between the surfaces. Other studies that have shown the impact of roughness descriptors on colloid deposition reported at least one order of magnitude difference in their value between smooth and rough surfaces (Stoll et al., 2016; Rasmuson et al., 2017). Although our Ra and Rq values were higher for the natural fracture rock surface than for the artificially created fracture surface, these differences were within the same order of magnitude and, thus, may not have impacted deposition. It was also shown that the roughness measurement depends on the size of the probe, and that measuring roughness on a length scale comparable to the colloid size is important in understanding the impact of roughness on colloid retention (Stoll et al., 2016). To characterize the surface roughness of our sample, the spatial resolution of the microscope scan was 10 μm in the x-y plane, an order of magnitude larger than our colloid size. This resolution was required to scan the entire surface of our samples, while the studies mentioned above performed surface roughness measurements using atomic force microscopes on much smaller surfaces. Thus, it remains

possible that the roughness of the natural fracture surface is higher at smaller scales, and we still have some uncertainty as to what the effective roughness at the colloid scale is.

In the inset of Fig. 2(d), we show the residual surface concentration of colloids over the natural fracture surface (at the end of the HH experiment) and reveal another interesting result. We observed regions on the surface with apparently very low residual concentrations of fluorescent colloids (appearing in dark green in the inset). These regions appear to be related to the presence of deposited minerals on the rock surface (black coating in Fig. 1(c)). As we see in Fig. 2(b) and in subsequent images not shown here, these regions remained relatively darker throughout the experiment, even at later times when we expected the colloids to reach low velocity zones and cover the entire surface. Therefore, while this low fluorescence could be attributed to low concentrations of deposited colloids, it could also be attributed to a reduction in fluorescence intensity by the darker background, and not to reduced deposition.

While we could not determine whether dark-coated rock surface regions in fact contributed to reduced deposition, it is still interesting to discuss the chemical differences between the rock surfaces. The elemental analysis of the bulk rock samples showed the presence of Ca, Si, P, O and C, suggesting that the artificially created surface was composed of calcium carbonates, calcium phosphates, and silicates. The analysis of the natural fracture surface additionally showed the presence of Mn, Ni, Fe, Al and Mg, suggesting that manganese and nickel oxides, and clay minerals coated the rock surface. These elements were also observed on the surfaces of natural coated fracture surfaces in chalk, in previous studies (Weisbrod et al., 1999).

Since manganese oxides were shown to have negative ζ-potential at the experimental pH of $\sim$6.5 (Zhang et al., 2017), they might have repelled the synthetic colloids, whose measured ζ-potential is -59 mV. However, since the ζ-potential of crushed-chalk powder, representing the pristine rock surface, is also negative (Zvikelsky et al., 2008), electrostatic repulsion alone may not explain the reduced deposition of colloids on the coated surface patches. Finally, the ζ-potential of glass under our experimental conditions (ionic strength and pH) is expected to be negative as well (Gu & Li, 2000). Therefore, we did not expect the surface charge of the glass cover to impact the overall flow and deposition of colloids in the cell.

4 Summary and conclusions

In this work, we describe an original experimental setup that allowed for direct visualization of colloid transport over a fractured rock sample. We used this setup and performed colloid transport experiments with two types of surfaces: (1) an artificially created fracture surface that exhibited lower physical heterogeneity and similar mineralogical composition to the bulk rock; and (2) a natural (active) fracture surface taken from a core drilled below the water table in the Negev Desert. The latter surface was characterized by spatially-varying fracture apertures and mineralogical composition. We show that aperture variation can create preferential colloid transport paths, or channeling, over the rock surface. We further show how the preferential transport pathways translated into an earlier emergence of colloids, by measuring their breakthrough curves. In addition, our colloid breakthrough curves exhibited significant retardation, as opposed to some other colloid transport studies (Becker et al., 1999; Zvikelsky & Weisbrod, 2006; Albaran et al., 2013; Stoll et al., 2016). We attribute this colloid retardation to the experimental conditions in our system, namely the ratio between fracture aperture and colloid diameter. While in our current setup, we could not verify the impact of surface mineralogical composition on colloid retention and attachment, our approach opens the way for more detailed investigation into their impact in future studies.

Acknowledgments

This work was funded by the Israel Science Foundation, under grant no. 165/17. OB acknowledges the generous support of Ben-Gurion University through the Marcus Postdoctoral Fellowship in Water Sciences, and thanks Emily Tran for helpful discussions. The data used to generate the figures in this paper can be found at `doi:10.5281/zenodo.5081121`. These include images, spreadsheets, and a MATLAB script for data analysis and plotting.

References

Albarran, N., Missana, T., Alonso, U., García-Gutiérrez, M., & López, T. (2013). Analysis of latex, gold and smectite colloid transport and retention in artificial fractures in crystalline rock. *Colloids and Surfaces A: Physicochemical and Engineering Aspects*, *435*, 115–126. doi: 10.1016/j.colsurfa.2013.02.002

Alonso, U., Missana, T., Patelli, A., Ceccato, D., Albarran, N., García-Gutiérrez, M., ... Rigato, V. (2009). Quantification of Au nanoparticles retention on a heterogeneous rock surface. *Colloids and Surfaces A: Physicochemical and Engineering Aspects*, *347*(1-3), 230–238. doi: 10.1016/j.colsurfa.2009.04.046

Becker, M. W., Reimus, P. W., & Vilks, P. (1999). Transport and attenuation of carboxylate-modified latex microspheres in fractured rock laboratory and field tracer tests. *Ground Water*, *37*(3), 387–395. doi: 10.1111/j.1745-6584.1999.tb01116.x

Berkowitz, B. (2002). Characterizing flow and transport in fractured geological media: A review. *Advances in Water Resources*, *25*(8-12), 861–884. doi: 10.1016/S0309-1708(02)00042-8

Bodin, J., Delay, F., & de Marsily, G. (2003). Solute transport in a single fracture with negligible matrix permeability: 1. fundamental mechanisms. *Hydrogeology Journal*, *11*(4), 418–433. doi: 10.1007/s10040-003-0268-2

Boutt, D. F., Grasselli, G., Fredrich, J. T., Cook, B. K., & Williams, J. R. (2006). Trapping zones: The effect of fracture roughness on the directional anisotropy of fluid flow and colloid transport in a single fracture. *Geophysical Research Letters*, *33*(21), L21402. doi: 10.1029/2006GL027275

Brewer, A., Dror, I., & Berkowitz, B. (2021). The mobility of plastic nanoparticles in aqueous and soil environments: A critical review. *ACS ES&T Water*, *1*(1), 48–57. doi: 10.1021/acsestwater.0c00130

Brown, S., Caprihan, A., & Hardy, R. (1998). Experimental observation of fluid flow channels in a single fracture. *Journal of Geophysical Research: Solid Earth*, *103*(B3), 5125–5132. doi: 10.1029/97JB03542

Chinju, H., Kuno, Y., Nagasaki, S., & Tanaka, S. (2001). Deposition behavior of polystyrene latex particles on solid surfaces during migration through an artificial fracture in a granite rock sample. *Journal of Nuclear Science and Technology*, *38*(6), 439–443. doi: 10.1080/18811248.2001.9715051

Chrysikopoulos, C. V., & James, S. C. (2003). Transport of neutrally buoyant and dense variably sized colloids in a two-dimensional fracture with anisotropic aperture. *Transport in Porous Media*, *51*(2), 191–210. doi: 10.1023/A:1021952226861

Cohen, M., & Weisbrod, N. (2018). Field scale mobility and transport manipulation of carbon-supported nanoscale zerovalent iron in fractured media. *Environmental Science and Technology*, *52*(14), 7849–7858. doi: 10.1021/acs.est.8b01226

Froidevaux, P., Steinmann, P., & Pourcelot, L. (2010). Long-term and long-range migration of radioactive fallout in a karst system. *Environmental Science and Technology*, *44*(22), 8479–8484. doi: 10.1021/es100954h

Gu, Y., & Li, D. (2000). The ζ-potential of glass surface in contact with aqueous solutions. *Journal of Colloid and Interface Science*, *226*(2), 328–339. doi: 10.1006/jcis.2000.6827

Horton, A. A., & Dixon, S. J. (2018). Microplastics: An introduction to environmental transport processes. *Wiley Interdisciplinary Reviews: Water*, *5*(2), e1268. doi: 10.1002/wat2.1268

James, S. C., & Chrysikopoulos, C. V. (2003). Effective velocity and effective dispersion coefficient for finite-sized particles flowing in a uniform fracture. *Journal of Colloid and Interface Science*, *263*(1), 288–295. doi: 10.1016/S0021-9797(03)00254-6

Kersting, A. B., Efurd, D. W., Finnegan, D. L., Rokop, D. J., Smith, D. K., & Thompson, J. L. (1999). Migration of plutonium in ground water at the Nevada Test Site. *Nature*, *397*(6714), 56–59. doi: 10.1038/16231

Kurra, S., Hifzur Rahman, N., Regalla, S. P., & Gupta, A. K. (2015). Modeling and optimization of surface roughness in single point incremental forming process. *Journal of Materials Research and Technology*, *4*(3), 304–313. doi: 10.1016/j.jmrt.2015.01.003

Kurtzman, D., Nativ, R., & Adar, E. M. (2007). Flow and transport predictions during multi-borehole tests in fractured chalk using discrete fracture network models. *Hydrogeology Journal*, *15*(8), 1629–1642. doi: 10.1007/s10040-007-0205-x

McCarthy, J. F., & Zachara, J. M. (1989). Subsurface transport of contaminants: binding to mobile and immobile phases in groundwater aquifers. *Environmental Science & Technology*, *23*(5), 496–502. doi: 10.1021/es00063a001

Medici, G., West, L. J., & Banwart, S. A. (2019). Groundwater flow velocities in a fractured carbonate aquifer-type: Implications for contaminant transport. *Journal of Contaminant Hydrology*, *222*, 1–16. doi: 10.1016/j.jconhyd.2019.02.001

Méheust, Y., & Schmittbuhl, J. (2001). Geometrical heterogeneities and permeability anisotropy of rough fractures. *Journal of Geophysical Research: Solid Earth*, *106*(B2), 2089–2102. doi: 10.1029/2000jb900306

Missana, T., Alonso, U., García-Gutiérrez, M., & Mingarro, M. (2008). Role of bentonite colloids on europium and plutonium migration in a granite fracture. *Applied Geochemistry*, *23*(6), 1484–1497. doi: 10.1016/j.apgeochem.2008.01.008

Mondal, P. K., & Sleep, B. E. (2012). Colloid transport in dolomite rock fractures: Effects of fracture characteristics, specific discharge, and ionic strength. *Environmental Science and Technology*, *46*(18), 9987–9994. doi: 10.1021/es301721f

Nativ, R., Adar, E., & Becker, A. (1999). Designing a monitoring network for contaminated ground water in fractured chalk. *Ground Water*, *37*(1), 38–47. doi: 10.1111/j.1745-6584.1999.tb00956.x

Rasmuson, A., Pazmino, E., Assemi, S., & Johnson, W. P. (2017). Contribution of nano- to microscale roughness to heterogeneity: Closing the gap between unfavorable and favorable colloid attachment conditions. *Environmental Science & Technology*, *51*(4), 2151–2160. doi: 10.1021/acs.est.6b05911

Rodrigues, S. N., & Dickson, S. E. (2015). The effect of matrix properties and preferential pathways on the transport of Escherichia Coli RS2-GFP in single, saturated, variable-aperture fractures. *Environmental Science and Technology*, *49*(14), 8425–8431. doi: 10.1021/acs.est.5b01578

Sahimi, M. (2011). *Flow and Transport in Porous Media and Fractured Rock*. Weinheim, Germany: Wiley-VCH Verlag GmbH & Co. KGaA. doi: 10.1002/9783527636693

Stoll, M., Huber, F., Darbha, G., Schill, E., & Schäfer, T. (2016). Impact of gravity, collector surface roughness and fracture orientation on colloid retention kinetics in an artificial fracture. *Journal of Colloid and Interface Science*, *475*, 171–183. doi: 10.1016/j.jcis.2016.04.045

Stoll, M., Huber, F., Trumm, M., Enzmann, F., Meinel, D., Wenka, A., ... Schäfer, T. (2019). Experimental and numerical investigations on the effect of frac-

ture geometry and fracture aperture distribution on flow and solute transport in natural fractures. *Journal of Contaminant Hydrology*, *221*, 82–97. doi: 10.1016/j.jconhyd.2018.11.008

Tang, X.-Y., & Weisbrod, N. (2010). Dissolved and colloidal transport of cesium in natural discrete fractures. *Journal of Environmental Quality*, *39*(3), 1066–1076. Retrieved from `http://www.ncbi.nlm.nih.gov/pubmed/20400602` doi: 10.2134/jeq2009.0345

Thoma, S. G., Gallegos, D. P., & Smith, D. M. (1992). Impact of fracture coatings on fracture/matrix flow interactions in unsaturated, porous media. *Water Resources Research*, *28*(5), 1357–1367. doi: 10.1029/92WR00167

Tran, E. L., Reimus, P., Klein-BenDavid, O., Teutsch, N., Zavarin, M., Kersting, A. B., & Weisbrod, N. (2020). Mobility of radionuclides in fractured carbonate rocks: Lessons from a field-scale transport experiment. *Environmental Science & Technology*, *54*(18), 11249–11257. doi: 10.1021/acs.est.0c03008

Tsang, C.-f., & Neretnieks, I. (1998). Flow channeling in heterogeneous fractured rocks. *Reviews of Geophysics*, *36*(2), 275–298. doi: 10.1029/97RG03319

Weisbrod, N., Meron, H., Walker, S., & Gitis, V. (2013). Virus transport in a discrete fracture. *Water Research*, *47*(5), 1888–1898. doi: 10.1016/j.watres.2013.01.009

Weisbrod, N., Nativ, R., Adar, E. M., & Ronen, D. (1999). Impact of intermittent rainwater and wastewater flow on coated and uncoated fractures in chalk. *Water Resources Research*, *35*(11), 3211–3222. doi: 10.1029/1999WR900194

Weisbrod, N., Nativ, R., Adar, E. M., Ronen, D., & Ben-Nun, A. (2000). Impact of coating and weathering on the properties of chalk fracture surfaces. *Journal of Geophysical Research: Solid Earth*, *105*(B12), 27853–27864. doi: 10.1029/2000jb900295

Zavarin, M., Roberts, S. K., Johnson, M. R., Hu, Q., Powell, B. A., Zhao, P., ... Pletcher, R. J. (2013). *Colloid-facilitated radionuclide transport in fractured carbonate rock from Yucca Flat, Nevada National Security Site* (Tech. Rep.). Livermore, California: Lawrence Livermore National Laboratory.

Zhang, H., Wu, A., Fu, H., Zhang, L., Liu, H., Zheng, S., ... Xu, Z. (2017). Efficient removal of Pb(ii) ions using manganese oxides: the role of crystal structure. *RSC Advances*, *7*(65), 41228–41240. doi: 10.1039/C7RA05955H

Zvikelsky, O., & Weisbrod, N. (2006). Impact of particle size on colloid transport in discrete fractures. *Water Resources Research*, *42*(12), W12S08. doi: 10.1029/2006WR004873

Zvikelsky, O., Weisbrod, N., & Dody, A. (2008). A comparison of clay colloid and artificial microsphere transport in natural discrete fractures. *Journal of Colloid and Interface Science*, *323*(2), 286–292. doi: 10.1016/J.JCIS.2008.04.035